

CrossMark
click for updatesCite this: *J. Mater. Chem. A*, 2015, 3,
8070Received 21st January 2015
Accepted 2nd March 2015

DOI: 10.1039/c5ta00502g

www.rsc.org/MaterialsA

Hydrated vanadium pentoxide with superior sodium storage capacity†

Qiulong Wei,^{‡a} Jin Liu,^{‡a} Wei Feng,^{‡a} Jinzhi Sheng,^a Xiacong Tian,^a Liang He,^{*a}
Qinyou An^b and Liqiang Mai^{*a}

Sodium ion batteries (SIBs), as potential candidates for large-scale energy storage systems, have attracted great attention from researchers. Herein, a $V_2O_5 \cdot nH_2O$ xerogel composed of thin acicular interconnected nanowire networks has been synthesized *via* a facile freeze-drying process. The interlayer spacing of $V_2O_5 \cdot nH_2O$ is larger than that of orthorhombic V_2O_5 due to the intercalation of water molecules into the layer structure. As the cathode of a SIB, $V_2O_5 \cdot nH_2O$ exhibits a high initial capacity of 338 mA h g^{-1} at 0.05 A g^{-1} and a high-rate capacity of 96 mA h g^{-1} at 1.0 A g^{-1} . On the basis of combining *ex-situ* XRD and FTIR spectroscopy, the Na^+ ion intercalation storage reactions are discussed in detail. By modeling calculations, the pseudocapacitive behavior makes a great contribution to the high capacities. Our work demonstrates that $V_2O_5 \cdot nH_2O$ with large interlayer spacing is a promising candidate for high capacity sodium-based energy storage.

Introduction

Electrochemical energy storage is becoming increasingly important in our daily life.^{1–5} Among the various energy storage technologies, rechargeable lithium ion batteries (LIBs) have been employed for mobile electronic devices and are now being extended to electric vehicles (EVs) and large-scale energy storage systems (ESS), owing to their high capacity and long cycle life.^{6–10} However, the large-scale demand for lithium would bring about a steep rise in price due to the low abundance of lithium on Earth.² Sodium is an abundant source and low cost, meanwhile, it has similar physical and chemical properties to lithium. Na^+ ions can also insert into and be extracted from electrodes, working as a “rocking-chair” battery like LIBs.^{11–14} Therefore, the development of large-scale and cheap ESS based on sodium ion batteries (SIBs) is a very reasonable choice.^{2,15–18} It is noted that the radius of the Na^+ ion is 97 pm, ~ 1.43 times larger than that of the Li^+ ion (68 pm), thus larger spacing is required to store Na^+ ions.² So, exploiting and optimizing

electrode materials with suitable spacing are critical for the development of SIBs.^{2,19}

Vanadium oxides, typical layered structure materials with high theoretical capacity and large abundance, have been extensively investigated for application in LIBs, while it is limited in sodium-based energy storage systems.^{20–24} Orthorhombic V_2O_5 (α - V_2O_5) with an interlayer spacing of $\sim 4.37 \text{ \AA}$ is not suitable for long-term reversible Na^+ ion insertion/extraction (Scheme 1a), since its capacity fades fast in the second cycle.^{12,19} However, layer-type vanadium oxides could intercalate various organic or inorganic composites with adjustable interlayer spacing.²⁵ Recently, single-crystalline bilayered V_2O_5 nanobelts with enlarged interlayer spacing ($\sim 11.53 \text{ \AA}$), reported by Su *et al.*, exhibited a largely improved sodium storage capacity (a high capacity of $231.4 \text{ mA h g}^{-1}$).¹² Water can also intercalate into vanadium pentoxide forming a double layer stacked along the *c*-axis (Scheme 1b).²⁶ The hydrated vanadium pentoxide ($V_2O_5 \cdot nH_2O$) displays an interlayer spacing range from 8.8 to 13.8 \AA , which can be adjusted by inserting different amounts of water.²³ This kind of large-spacing bilayer $V_2O_5 \cdot nH_2O$ exhibited a large capacity of $\sim 300 \text{ mA h g}^{-1}$ for Li^+ ion intercalation.²⁷ In addition, larger ions (Na^+ and K^+) can also insert into the layers in aqueous electrolytes.^{28,29} However, its application to sodium storage in the organic electrolyte system and the detailed mechanism remain largely unexplored.

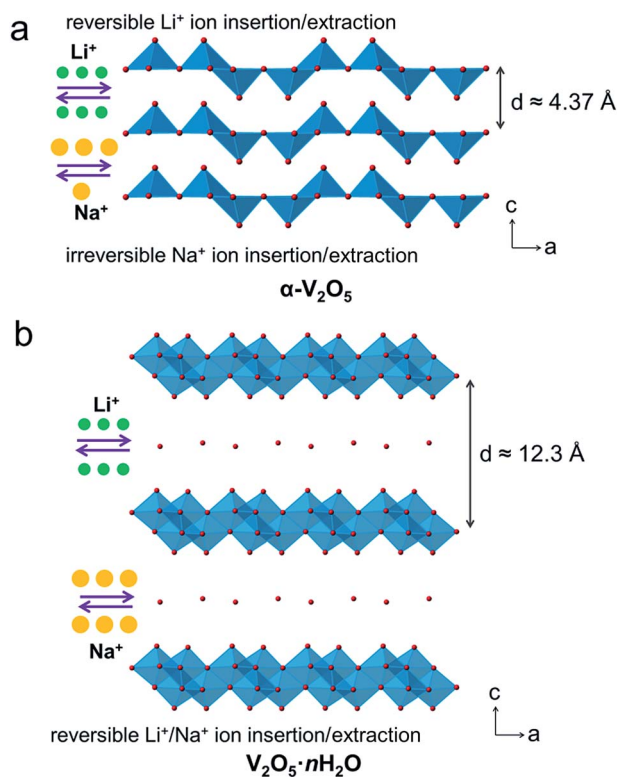
Herein, a $V_2O_5 \cdot nH_2O$ xerogel was synthesized through a facile freeze-drying process. The $V_2O_5 \cdot nH_2O$ cathode displays excellent sodium storage ability with a high capacity of 338 mA h g^{-1} at a current density of 0.05 A g^{-1} , which is much higher than that of α - V_2O_5 . Benefiting from the layer structure,

^aState Key Laboratory of Advanced Technology for Materials Synthesis and Processing, Wuhan University of Technology, Wuhan 430070, Hubei, China. E-mail: mlq518@whut.edu.cn; hel@whut.edu.cn

^bCullen College of Engineering, Department of Electrical & Computer Engineering, University of Houston, Houston, USA

† Electronic supplementary information (ESI) available: XRD pattern and SEM images of α - V_2O_5 , discharge-charge curves and *ex-situ* XRD pattern of the α - V_2O_5 cathodes in the SIB test collected at various charge/discharge states, Coulombic efficiency of the $V_2O_5 \cdot nH_2O$ and α - V_2O_5 cathodes in the SIB test, LIB performance of the $V_2O_5 \cdot nH_2O$ and α - V_2O_5 cathodes, *ex-situ* XRD pattern and FTIR spectra of the $V_2O_5 \cdot nH_2O$ cathodes in the LIB test collected at various charge/discharge states. See DOI: 10.1039/c5ta00502g

‡ These authors contributed equally to this work.



Scheme 1 The structural models of $\alpha\text{-V}_2\text{O}_5$ (a) and $\text{V}_2\text{O}_5 \cdot n\text{H}_2\text{O}$ (b) viewed along the [010] direction. $\alpha\text{-V}_2\text{O}_5$ is not suitable for reversible Na^+ ion insertion/extraction, while $\text{V}_2\text{O}_5 \cdot n\text{H}_2\text{O}$ is beneficial to reversible and rapid Na^+ ion insertion/extraction.

it also exhibits excellent high-rate lithium storage ability with a high capacity of 162 mA h g^{-1} at 6.0 A g^{-1} . Further, the Na^+/Li^+ ions intercalation storage reactions are investigated systematically through *ex-situ* XRD and FTIR analyses. This work demonstrates that $\text{V}_2\text{O}_5 \cdot n\text{H}_2\text{O}$ with large interlayer spacing is a promising candidate for the development of high capacity sodium-based as well as lithium-based energy storage.

Experimental section

Materials synthesis

Synthesis of V_2O_5 sols. The V_2O_5 sols were prepared by a melt quenching process as described previously.^{30,31} In brief, V_2O_5 powder (30 g) was placed in a ceramic crucible and heated in air at $800 \text{ }^\circ\text{C}$ for 20 min at a rate of $10 \text{ }^\circ\text{C min}^{-1}$, resulting in the molten liquid. Then, the molten liquid was quickly poured into distilled water with stirring, and the suspensions were obtained. The suspensions were heated to the water boiling point beforehand and then naturally cooled to room temperature. Finally, the suspension was filtered and brownish V_2O_5 sols were obtained.

Synthesis of $\text{V}_2\text{O}_5 \cdot n\text{H}_2\text{O}$ xerogel. The as-prepared sol was frozen and then underwent a freeze-drying process to remove residual water. Finally, the $\text{V}_2\text{O}_5 \cdot n\text{H}_2\text{O}$ xerogel was dried at $120 \text{ }^\circ\text{C}$ in air for another 5 hours.

Synthesis of $\alpha\text{-V}_2\text{O}_5$ xerogel. For comparison, the crystalline $\alpha\text{-V}_2\text{O}_5$ was obtained after annealing the $\text{V}_2\text{O}_5 \cdot n\text{H}_2\text{O}$ xerogel at $450 \text{ }^\circ\text{C}$ in air for 2 hours.

Materials characterization

X-ray diffraction (XRD) measurements were performed to investigate the crystallographic information using a D8 Advance X-ray diffractometer with a non-monochromatic $\text{Cu K}\alpha$ X-ray source. Fourier transformed infrared (FTIR) transmittance spectra were recorded using a 60-SXB IR spectrometer. X-ray photoelectron spectroscopy (XPS) measurements were performed using a VG MultiLab 2000 instrument. TG analysis was performed using a NETZSCH-STA449c/3/G thermoanalyzer. Brunauer–Emmett–Teller (BET) surface areas were measured using a Tristar II 3020 instrument. The morphology and structure of the product were observed through scanning electron microscopy (SEM, JEOL-7100F) and transmission electron microscopy (TEM, JEM-2100F microscope).

Electrochemical measurements

The electrochemical properties were evaluated by assembling 2016 coin cells in an argon-filled glove box ($\text{O}_2 \leq 1 \text{ ppm}$ and $\text{H}_2\text{O} \leq 1 \text{ ppm}$). For the preparation of the electrodes, 70% active material, 20% acetylene black and 10% poly(tetrafluoroethylene) (PTFE) were mixed in isopropanol. Then, the mixed clay was rolled using a roller mill to form a freestanding film. Then, the film was cut into disks with a diameter of 8 mm and dried. The loading of the active material was $2\text{--}3 \text{ mg cm}^{-2}$. For the fabrication of the sodium batteries, sodium pellets were used as the anode, a 1 M solution of NaClO_4 in ethylene carbon (EC)/propylene carbonate (PC) with a volume ratio of 1 : 1 was used as the electrolyte. For the fabrication of the lithium batteries, lithium pellets were used as the anode, and a 1 M solution of LiPF_6 in EC/dimethyl carbonate (DMC) with a volume ratio of 1 : 1 was used as the electrolyte. Galvanostatic charge–discharge cycling was studied with a multi-channel battery testing system (LAND CT2001A). Cyclic voltammetry (CV) and electrochemical impedance spectroscopy (EIS) were performed with an electrochemical workstation (Autolab PGSTAT302N).

Results and discussion

The XRD pattern of the as-prepared product (Fig. 1a) shows the typical (00 l) reflection peaks, which are consistent with those of the layered structure of $\text{V}_2\text{O}_5 \cdot n\text{H}_2\text{O}$ (JCPDF no. 40-1296).^{26,28} The hydrated V_2O_5 has a layered structure consisting of VO_6 octahedral layers stacked along the c -axis (Scheme 1b).²⁶ This structure was also confirmed by the FTIR spectrum, as shown in Fig. 1b. The peaks centered at 503 and 757 cm^{-1} are assigned to the V–O–V stretching modes and that at 1013 cm^{-1} to the V=O stretching band.³¹ The absorption bands at 3426 and 1637 cm^{-1} are attributed to the stretching and bending modes of the O–H vibrations, respectively, which confirms the intercalation of water molecules into the vanadium oxide layers.^{31,32} The TG curve (Fig. 1c) of the hydrated sample exhibits obvious weight

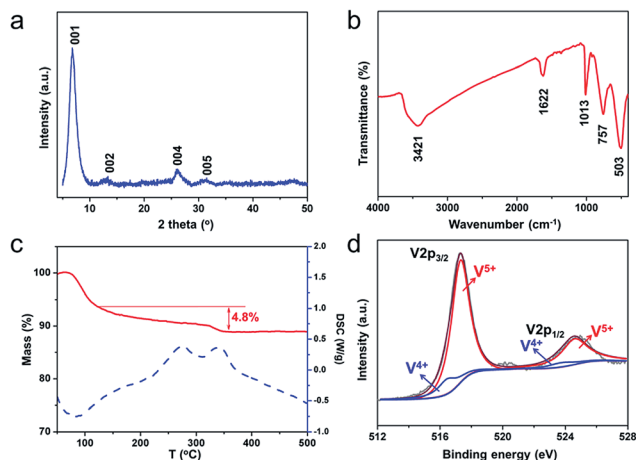


Fig. 1 XRD pattern (a), FTIR spectrum (b), TGA profiles (c) and V2p XPS spectra (d) of the as-synthesized $V_2O_5 \cdot nH_2O$ xerogel.

loss slopes. The total weight loss from $V_2O_5 \cdot nH_2O$ to crystalline α - V_2O_5 (annealed at 450 °C, Fig. S1†) is 4.8%, which can be estimated to $n \approx 0.55$ ($V_2O_5 \cdot nH_2O \rightarrow V_2O_5 + nH_2O$).

To identify the chemical composition of the as-prepared hydrated vanadium oxide, XPS was carried out. The V2p_{3/2} state has a broad peak and can be deconvoluted into two synthetic peaks.³³ The deconvoluted V2p_{3/2} binding energies of 517.3 and 516.5 eV are consistent with the typically reported values for V⁵⁺ and V⁴⁺.¹³ The V⁴⁺/V⁵⁺ ratio is \sim 16.8%, indicating the presence of oxygen vacancies in the lattice.³⁴ The existence of V⁴⁺ is due to the reduction reaction between molten V_2O_5 and cold water during the preparation process of the vanadium oxide sols. A previous study demonstrated that such oxygen vacancies can enhance the electrochemical performance.³⁴ SEM and TEM were used to characterize the morphology and detailed structure of the samples. The as-dried xerogel is a fluffy sponge (inset

of Fig. 2a). The SEM images (Fig. 2a and b) show a thin large-area two-dimensional flake structure, which is due to the ice-template effect during the freeze-drying process.³⁵ As shown in the TEM images (Fig. 2c and d), the flakes are composed of thin acicular nanowires with lots of pores. Additionally, nitrogen adsorption-desorption was further measured. The xerogel has a BET surface area of 17.6 m² g⁻¹ and a pore volume of 0.034 cm³ g⁻¹.

Detailed electrochemical measurements were conducted to investigate the sodium storage performance. The electrochemical performances were evaluated firstly by cyclic voltammetry (CV), as shown in Fig. 3a. The $V_2O_5 \cdot nH_2O$ cathode displays three couples of distinct redox peaks in the potential range of 1.0–4.0 V, corresponding to the multi-electron reaction along with the changing of various vanadium valence states. The three anodic peaks situated at 3.71, 3.17 and 2.14 V correspond to the cathodic peaks at 3.44, 2.40 and 1.61 V. Fig. 3b shows the charge-discharge curves at a current density of 0.1 A g⁻¹. A high capacity of 306 mA h g⁻¹ is obtained at a current density of 0.1 A g⁻¹ (Fig. 3b), according to about 2.32 Na⁺ ions per unit formula. The calculation is based on the equation $n = (3.6MC)/F$, where n represents the inserted ion amount (mol), F represents the Faraday constant (C mol⁻¹), C represents the capacity (mA h g⁻¹), and M represents the molecular weight (g mol⁻¹).³⁶ This capacity is much higher than those of the α - V_2O_5 xerogel (170 mA h g⁻¹) (Fig. 3c), V_2O_5 hollow nanospheres (230.0 mA h g⁻¹ at 23 mA g⁻¹ at 1.0–4.2 V),¹⁹ bilayered V_2O_5 nanobelts (231.4 mA h g⁻¹ at 80 mA g⁻¹ at 1.0–4.0 V)¹² and V_2O_5/C nanocomposites (170 mA h g⁻¹ at 40 mA g⁻¹ at 1.5–3.8 V);¹³ the details are listed in Table S1.† The second discharge capacity of the $V_2O_5 \cdot nH_2O$ cathode is 300 mA h g⁻¹. A capacity loss of only 6 mA h g⁻¹ indicates a highly reversible reaction during the Na⁺ ion insertion/extraction. However, for the α - V_2O_5 cathode, the capacity quickly fades to 71 mA h g⁻¹ in the second cycle, corresponding to a capacity loss of

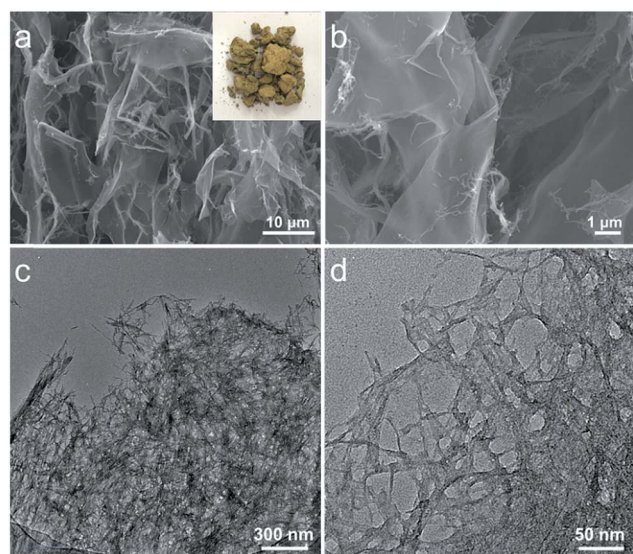


Fig. 2 SEM images (a and b) and TEM images (c and d) of the $V_2O_5 \cdot nH_2O$ xerogel. Inset of (a) is the optical image of the xerogel.

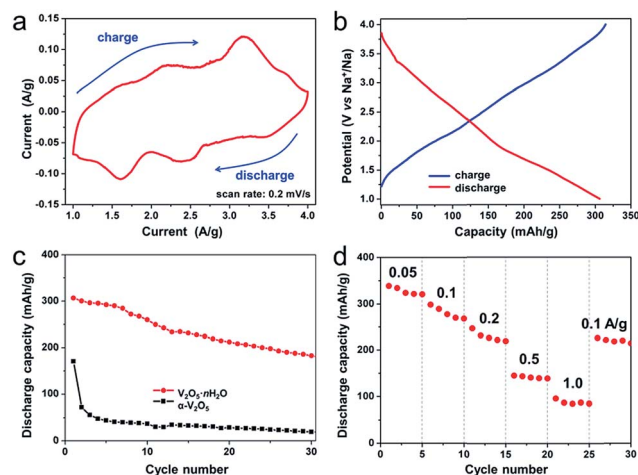


Fig. 3 SIB performance of the $V_2O_5 \cdot nH_2O$ cathode. CV curves (a) and discharge-charge curves at current density of 0.1 A g⁻¹ (b). Cycling performance at the current density of 0.1 A g⁻¹ (c) and the rate performance (d).

99 mA h g⁻¹; the large capacity loss is due to the fact that the phase transition (from the α -V₂O₅ phase to the NaV₂O₅ phase) is irreversible (Fig. S2†).^{12,19} The Coulombic efficiency of the V₂O₅·*n*H₂O cathode is around 97.5% in the overall battery testing process (Fig. S3†), which is much higher than that of the α -V₂O₅ cathode. The rate performance shows that V₂O₅·*n*H₂O delivers a capacity of 338 mA h g⁻¹ at 0.05 A g⁻¹ and considerable rate capacities of 145 and 96 mA h g⁻¹ at 0.5 and 1.0 A g⁻¹, respectively (Fig. 3d). The good rate capability is due to the large interlayer spacing which is helpful for the storage of Na⁺ ions.¹²

The lithium storage performance was also measured, as displayed in Fig. S4.† The as-prepared V₂O₅·*n*H₂O cathode delivers an initial discharge capacity of 340 mA h g⁻¹ at 0.1 A g⁻¹ at 1.5–4.0 V vs. Li⁺/Li, corresponding to ~2.56 Li⁺ ions per unit formula (Fig. S4b†). The cycling performance measured at a current density of 0.5 A g⁻¹ is shown in Fig. S4c.† The initial capacity is 311 mA h g⁻¹ at 1.5–4.0 V and the capacity of 227 mA h g⁻¹ was retained after 50 cycles. The rate performance with a progressively increasing current density (ranging from 0.1 to 6.0 A g⁻¹) was measured (Fig. S4d†) and a high capacity of 162 mA h g⁻¹ was achieved at 6.0 A g⁻¹ at 1.5–4.0 V. Although suffering from the rapid change of the current density, the electrode exhibits a stable capacity at each current density. The rate capacity is much higher than that of the α -V₂O₅ cathodes (Fig. S5†), indicating that the large interlayer spacing is beneficial to the rapid ion diffusion.

It is known that the surface reaction is usually faster than that in the inner diffusion region. Therefore, when a battery material is engineered at the nanoscale, most of the ion storage sites are on the surface or in the near-surface region, where capacitance will occur, leading to a good rate performance.³⁷ Since the xerogel consists of very thin acicular nanowires and delivers an excellent high-rate performance for both lithium and sodium storage, it is supposed that the cathode may exhibit significant capacitance. So, it is necessary to find out the different charge-storage mechanisms for the diffusion-controlled Faradaic reaction and the capacitive behavior (non-Faradaic electrical double layer capacitance and pseudocapacitance). Gradually increasing voltammetric scan rates are used to calculate and identify the capacitive contribution.³⁸ Fig. 4a displays the cyclic voltammetry (CV) curves of SIBs at various rates. For the calculation, the total current response (*i*) at a fixed potential (*V*) can be described as the combination of these two separate mechanisms (eqn (1)):^{13,38}

$$i(V) = k_1v + k_2v^{1/2} \quad (1)$$

where k_1v represents the total capacitive contribution, while $k_2v^{1/2}$ stands for the contribution of the diffusion-controlled Faradaic intercalation process. The linear plot of $i/v^{1/2}$ versus $v^{1/2}$ was used to determine k_1 and k_2 . Thus, the diffusion processes and those from capacitive effects can be distinguished, as previously demonstrated.^{39,40} Fig. 4b and S7† show the total stored charge for SIBs and LIBs at various scan rates, respectively. The diffusion contribution is 72.8% at 0.2 mV s⁻¹, while it decreases with increasing scan rate from 0.2 to 1.0 mV s⁻¹ and the proportion of the capacitive contribution increases

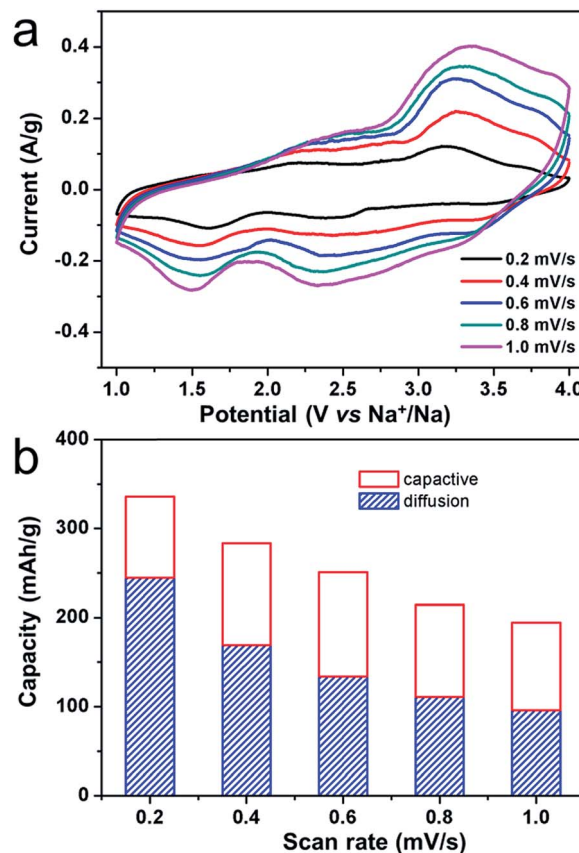


Fig. 4 CV curves (a) and corresponding capacity contribution (b) of the total stored charge at various scan rates for the SIB test.

(Fig. S6†). The diffusion contribution for SIBs is 49.3% at 1.0 mV s⁻¹. This behavior was also observed in the LIB testing (Fig. S7†). These results show that the capacitive charge storage accounts for a significant proportion of the total capacity (for both sodium and lithium storage), particularly at high scan rates. Notice that the capacitive contribution is related to the surface area and crystal structure.^{39,40} However, the surface area of the as-synthesized xerogel is only 17.6 m² g⁻¹. Therefore, the result of the high-rate capacity and pseudocapacitive behavior is due to the fact that ions can be rapidly stored in the large layer space of the hydrated vanadium oxide structure.

In order to further investigate the layer structure changes of the V₂O₅·*n*H₂O cathodes during charging and discharging, *ex-situ* XRD patterns and FTIR spectra of the electrodes at different charge states were obtained (Fig. 5).^{12,28,29} The main (001) reflection peak is visibly shifting toward higher angles along with the decrease in crystallinity (the intensity ratio of (001)/*PTFE is reduced) during the discharge process (Fig. 5a). The shifting to higher angles reflects the decrease of interlayer spacing, which is because the intercalation of Na⁺ ions enhances the coordination reaction with the stacked layer and makes the interlayer spacing contract drastically.^{28,29} These phenomena are also observed after the intercalation of Li⁺ ions (Fig. S8†). The related calculated d_{001} values at each state are displayed in Fig. 5b. The reduction of interlayer spacing becomes negligible after more ions intercalate. For the

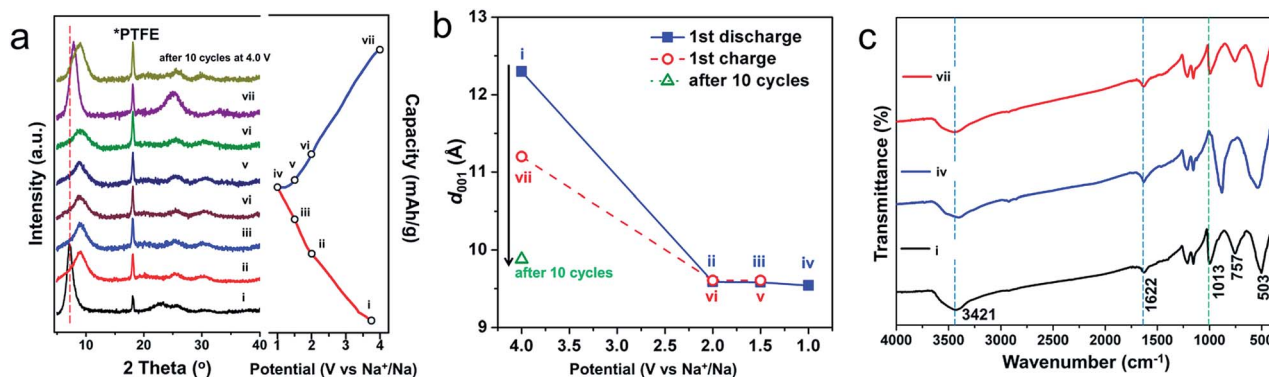


Fig. 5 *Ex-situ* XRD patterns (a), related d_{001} value changes (b) and FTIR spectra (c) of the cathodes in the SIB test collected at various charge/discharge states: (i) before cycle, (ii) discharged to 2 V, (iii) discharged to 1.5 V, (iv) discharged to 1.0 V, (v) re-charged to 1.5 V, (vi) re-charged to 2.0 V and (vii) re-charged to 4.0 V.

following charging process, the extraction of Na^+ ions restores the layer structure of the hydrated vanadium pentoxide. In the FTIR spectra, after a deep discharge (Fig. 5c(iv)), the red shift of the V=O stretching bond demonstrates the reduction of V^{5+} to V^{4+} ,⁴¹ while the peak of the out-of-plane V-O-V vibrations (503 cm^{-1}) almost remains unchanged during cycling, indicating the stability of the vanadium oxide layer after Na^+ ion insertion. These bands were reproduced after the extraction of Na^+ ions (Fig. 5c(vii)). The above data indicate that the layer of $\text{V}_2\text{O}_5 \cdot n\text{H}_2\text{O}$ is shrinking/expanding along with the Na^+ ion insertion/extraction and it is reversible, which is different from the irreversible phase transition of $\alpha\text{-V}_2\text{O}_5$ (Fig. S2†). It is noted that the interlayer spacing of $\text{V}_2\text{O}_5 \cdot n\text{H}_2\text{O}$ was not totally recovered to its initial state (with a very small reduction). The collapsing of the layer structure becomes worse after 10 cycles, while it seems that the structure is more stable after repeated Li^+ ion insertion/extraction (Fig. S8a and b†). Therefore, the shrinkage and collapse of the layer structure for long-term cycling may be the main reason for the fast capacity fading of SIBs. Further repressing the large shrinkage/expansion during the Na^+ ion intercalation/extraction would improve the cycling stability. In addition, it is important to identify and discuss the extraction of structural water during cycling. As demonstrated previously, the interlayer spacing of $\text{V}_2\text{O}_5 \cdot n\text{H}_2\text{O}$ is closely related to the amount of intercalated water.²³ Therefore, the good recovery of the interlayer spacing of $\text{V}_2\text{O}_5 \cdot n\text{H}_2\text{O}$ after one full cycle (Fig. S8b†) indicates the resistance of water in the material during cycling. In addition, the bands at 1622 and 3421 cm^{-1} in the FTIR spectra still exist (Fig. 5c), which may also reflect that the crystal water is not totally exchanged during the ion intercalation.^{23,32}

Conclusions

The $\text{V}_2\text{O}_5 \cdot n\text{H}_2\text{O}$ xerogel composed of thin acicular interconnected nanowire networks was synthesized through a facile freeze-drying process. The $\text{V}_2\text{O}_5 \cdot n\text{H}_2\text{O}$ cathode exhibits an excellent electrochemical performance for SIBs as well as LIBs, which are correlated to its large interlayer spacing and the

shortened ion diffusion pathways of the ultrathin acicular nanowires. This open layer structure provides continuous channels for Na^+ ion insertion/extraction. For sodium storage, the $\text{V}_2\text{O}_5 \cdot n\text{H}_2\text{O}$ cathode delivers a high initial capacity of 338 mA h g^{-1} at 0.05 A g^{-1} and a high-rate capacity of 96 mA h g^{-1} at 1.0 A g^{-1} . Computational modeling indicates that the pseudocapacitive behavior accounts for a significant portion of the total capacity. Verified by the *ex-situ* XRD and FTIR analysis, the shrinkage and collapse of the layer structure during long-term cycling is one of the main reasons for the capacity fading. Our work demonstrates that $\text{V}_2\text{O}_5 \cdot n\text{H}_2\text{O}$ with large interlayer spacing is a promising candidate for the development of high capacity sodium-based energy storage. We believe that adjusting the interlayer spacing by ion pre-exchange would lead to a great advance in stabilizing the structure and improving the cycling performance.

Acknowledgements

This work was supported by the National Basic Research Program of China (2013CB934103, 2012CB933003), the International Science and Technology Cooperation Program of China (2013DFA50840), the National Science Fund for Distinguished Young Scholars (51425204), the Natural Science Foundation of Hubei Province (2014CFA035), the Fundamental Research Funds for the Central Universities (2014-YB-001, 2014-IV-062, 2014-IV-147), and the Students Innovation and Entrepreneurship Training Program (20141049701006). Thanks to Prof. D.Y. Zhao of Fudan University and Prof. C. M. Lieber of Harvard University for strong support and stimulating discussions. The authors are grateful to Yubin Sun of the Center for Materials Research and Analysis of Wuhan University of Technology for materials characterization.

References

- 1 L. Mai, X. Tian, X. Xu, L. Chang and L. Xu, *Chem. Rev.*, 2014, **114**, 11828–11862.
- 2 N. Yabuuchi, K. Kubota, M. Dahbi and S. Komaba, *Chem. Rev.*, 2014, **114**, 11636–11682.

- 3 H. Pan, Y.-S. Hu and L. Chen, *Energy Environ. Sci.*, 2013, **6**, 2338–23860.
- 4 Q. Zhang, E. Uchaker, S. L. Candelaria and G. Cao, *Chem. Soc. Rev.*, 2013, **42**, 3127–3171.
- 5 S. Chen, J. Duan, M. Jaroniec and S. Z. Qiao, *J. Mater. Chem. A*, 2013, **1**, 9409–9413.
- 6 M. Armand and J.-M. Tarascon, *Nature*, 2008, **451**, 652–657.
- 7 J. B. Goodenough and K. S. Park, *J. Am. Chem. Soc.*, 2013, **135**, 1167–1176.
- 8 F.-F. Cao, Y.-G. Guo and L.-J. Wan, *Energy Environ. Sci.*, 2011, **4**, 1634–1642.
- 9 H. Liu, S. Chen, G. Wang and S. Z. Qiao, *Chem.–Eur. J.*, 2013, **19**, 16897–16901.
- 10 Y. Wang, M. Xu, Z. Peng and G. Zheng, *J. Mater. Chem. A*, 2013, **1**, 13222–13226.
- 11 N. Yabuuchi, M. Kajiyama, J. Iwatate, H. Nishikawa, S. Hitomi, R. Okuyama, R. Usui, Y. Yamada and S. Komaba, *Nat. Mater.*, 2012, **11**, 512–517.
- 12 D. Su and G. Wang, *ACS Nano*, 2013, **7**, 11218–11226.
- 13 V. Raju, J. Rains, C. Gates, W. Luo, X. Wang, W. F. Stickle, G. D. Stucky and X. Ji, *Nano Lett.*, 2014, **14**, 4119–4124.
- 14 S. Tepavcevic, H. Xiong, V. R. Stamenkovic, X. Zuo, M. Balasubramanian, V. B. Prakapenka, C. S. Johnson and T. Rajh, *ACS Nano*, 2011, **6**, 530–538.
- 15 C. Luo, Y. Xu, Y. Zhu, Y. Liu, S. Zheng, Y. Liu, A. Langrock and C. Wang, *ACS Nano*, 2013, **7**, 8003–8010.
- 16 Y. Kim, Y. Park, A. Choi, N. S. Choi, J. Kim, J. Lee, J. H. Ryu, S. M. Oh and K. T. Lee, *Adv. Mater.*, 2013, **25**, 3045–3049.
- 17 Y. Fang, L. Xiao, J. Qian, X. Ai, H. Yang and Y. Cao, *Nano Lett.*, 2014, **14**, 3539–3543.
- 18 H. He, G. Jin, H. Wang, X. Huang, Z. Chen, D. Sun and Y. Tang, *J. Mater. Chem. A*, 2014, **2**, 3563–3570.
- 19 D. W. Su, S. X. Dou and G. X. Wang, *J. Mater. Chem. A*, 2014, **2**, 11185–11194.
- 20 N. A. Chernova, M. Roppolo, A. C. Dillon and M. S. Whittingham, *J. Mater. Chem.*, 2009, **19**, 2526.
- 21 L. Mai, Q. Wei, Q. An, X. Tian, Y. Zhao, X. Xu, L. Xu, L. Chang and Q. Zhang, *Adv. Mater.*, 2013, **25**, 2969–2973.
- 22 Q. An, Q. Wei, L. Mai, J. Fei, X. Xu, Y. Zhao, M. Yan, P. Zhang and S. Huang, *Phys. Chem. Chem. Phys.*, 2013, **15**, 16828–16833.
- 23 M. S. Whittingham, *Chem. Rev.*, 2004, **104**, 4271–4302.
- 24 X. Huang, X. Rui, H. H. Hng and Q. Yan, *Part. Part. Syst. Charact.*, 2014, DOI: 10.1002/ppsc.201400125.
- 25 D. McNulty, D. N. Buckley and C. O'Dwyer, *J. Power Sources*, 2014, **267**, 831–873.
- 26 V. Petkov, P. N. Trikalitis, E. S. Bozin, S. J. L. Billinge, T. Vogt and M. G. Kanatzidis, *J. Am. Chem. Soc.*, 2002, **124**, 10157–10162.
- 27 G. Sudant, E. Baudrin, B. Dunn and J.-M. Tarascon, *J. Electrochem. Soc.*, 2004, **151**, A666–A671.
- 28 Q. T. Qu, Y. Shi, L. L. Li, W. L. Guo, Y. P. Wu, H. P. Zhang, S. Y. Guan and R. Holze, *Electrochem. Commun.*, 2009, **11**, 1325–1328.
- 29 Q. T. Qu, L. L. Liu, Y. P. Wu and R. Holze, *Electrochim. Acta*, 2013, **96**, 8–12.
- 30 L. Mai, W. Chen, Q. Xu, Q. Zhu, C. Han and J. Peng, *Solid State Commun.*, 2003, **126**, 541–543.
- 31 W. Chen, *Mater. Lett.*, 2004, **58**, 2275–2278.
- 32 E. C. Zampronio, T. A. F. Lassali and H. P. Oliveira, *Electrochim. Acta*, 2005, **51**, 257–267.
- 33 G. Wang, X. Lu, Y. Ling, T. Zhai, H. Wang, Y. Tong and Y. Li, *ACS Nano*, 2012, **6**, 10296–10302.
- 34 D. Liu, Y. Liu, A. Pan, K. P. Nagle, G. T. Seidler, Y.-H. Jeong and G. Cao, *J. Phys. Chem. C*, 2011, **115**, 4959–4965.
- 35 L. Qiu, J. Z. Liu, S. L. Chang, Y. Wu and D. Li, *Nat. Commun.*, 2012, **3**, 1241.
- 36 X. Tian, X. Xu, L. He, Q. Wei, M. Yan, L. Xu, Y. Zhao, C. Yang and L. Mai, *J. Power Sources*, 2014, **255**, 235–241.
- 37 P. Simon, Y. Gogotsi and B. Dunn, *Science*, 2014, **343**, 1210–1211.
- 38 I. E. Rauda, V. Augustyn, L. C. Saldarriaga-Lopez, X. Chen, L. T. Schelhas, G. W. Rubloff, B. Dunn and S. H. Tolbert, *Adv. Funct. Mater.*, 2014, **24**, 6717–6728.
- 39 V. Augustyn, J. Come, M. A. Lowe, J. W. Kim, P. L. Taberna, S. H. Tolbert, H. D. Abruna, P. Simon and B. Dunn, *Nat. Mater.*, 2013, **12**, 518–522.
- 40 J. W. Kim, V. Augustyn and B. Dunn, *Adv. Energy Mater.*, 2012, **2**, 141–148.
- 41 K. Xu, S. Hu, C. Wu, C. Lin, X. Lu, L. Peng, J. Yang and Y. Xie, *J. Mater. Chem.*, 2012, **22**, 18214–18220.